ACS APPLIED MATERIALS & INTERFACES

Research Article

www.acsami.org

Improved Morphology Control Using a Modified Two-Step Method for Efficient Perovskite Solar Cells

Dongqin Bi,[†] Ahmed M. El-Zohry,[†] Anders Hagfeldt,[†,‡] and Gerrit Boschloo*[,†]

[†]Department of Chemistry-Ångström Laboratory, Uppsala University, Box 532, SE 751 20 Uppsala, Sweden

[‡]School of Chemical Engineering, Sungkyunkwan University, Suwon 440-746, Korea

Supporting Information

ABSTRACT: A two-step wet chemical synthesis method for methylammonium lead(II) triiodide ($CH_3NH_3PbI_3$) perovskite is further developed for the preparation of highly reproducible solar cells, with the following structure: fluorine-doped tin oxide (FTO)/TiO_2 (compact)/TiO_2 (mesoporous)/$CH_3NH_3PbI_3$/spiro-OMeTAD/Ag. The morphology of the perovskite layer could be controlled by careful variation of the processing conditions. Specifically, by modifying the drying process and inclusion of a dichloromethane treatment, more uniform films could be prepared, with longer emission lifetime in the perovskite material and longer electron lifetime in solar cell devices, as well as faster electron transport and enhanced charge collection at the selective contacts. Solar cell efficiencies up to 13.5% were obtained.

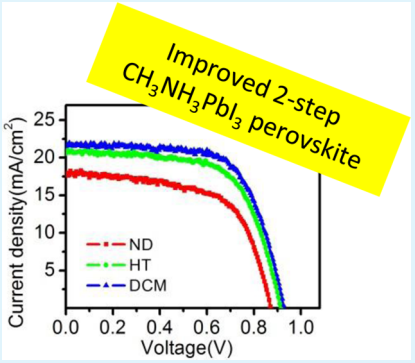

KEYWORDS: *photovoltaic, methylammonium lead(ii) triiodide, solution-processed semiconductor, mesoporous TiO_2, dichloromethane, emission lifetime*

Developing cost-effective and environmentally benign green energy remains a great challenge for scientific development.[1,2] The emerging photovoltaics are developing at a rapid pace. Crystalline silicon solar cells have been continuously advancing in efficiency and cost-reduction over the last decades.[3] However, there are many other solar cell technologies that promise even lower costs, and these range from thin-film solar cells (CdTe or Cu(InGa)Se_2, InGaAs)[4] to solution-processed solar cells, including dye-sensitized solar cells,[5] polymer solar cells,[6] and quantum dot solar cells.[7] Since the thin-film solar cells need high vacuum and high temperature or some rare element, solution-processed solar cells seem to be attractive. However, because of fundamental energy losses associated with charge separation in a low dielectric or energetically disordered medium, their theoretical maximum performances fall below those of inorganic thin-film solar cells.[8] The breakthrough discovery of perovskite $CH_3NH_3PbX_3$ (X = Cl, Br, I)-based solar cells sheds new light on developing cost-effective and high efficient devices. The highest power conversion efficiency (PCE) was confirmed from KRICT at 17.9%.[9] Generally, there are four methods, including spin-coating,[10] vacuum vapor deposition,[11] two-step deposition technique,[12,13] and patterning thin film[14] to prepare the hybrid perovskite film.[15] So far, in the application field of perovskite solar cells, $CH_3NH_3PbX_3$ is formed either by a so-called one-step or two-step method. For the one-step method, it can either be solution-processed or vapor-processed. For example, PbX_2 and CH_3NH_3X are mixed in *N*,*N*-dimethylformamide (DMF) or γ-butyrolactone (GBL) to make the precursor solution, followed by spin-coating to get $CH_3NH_3PbX_3$ film.[16−18] In addition, $CH_3NH_3PbI_{3-x}Cl_x$ was reported to be formed by dual-source vapor deposition, which has yielded 15% power conversion efficiency by using a planar structure.[19] For the two-step method, a PbI_2 film is first deposited, and $CH_3NH_3PbI_3$ is formed by dipping the film into CH_3NH_3I solution or exposure to CH_3NH_3I vapor.[20−22] Previous reports showed that larger crystals of perovskite with various sizes, ranging from hundreds of nanometers to microisland structures are formed when using the one-step solution-processed method.[20,23] Relatively uniform perovskite crystals are formed by using a wet-chemical two-step method, which is favorable for making highly reproducible solar cells with a highest value of 15%.[20] Reproducibility in the two-step method appears to be better than for other methods.[23−28]

RESULTS AND DISCUSSION

The general procedure of the two-step method for synthesis of $CH_3NH_3PbI_3$ perovskite is as follows: deposition of PbI_2 film by spin coating → dipping into a CH_3NH_3I solution in isopropanol (IPA) to form perovskite → washing with IPA to remove excess CH_3NH_3I → drying → heat treatment.

During the washing process with IPA and the following drying period, some dissolution of $CH_3NH_3PbI_3$ can occur. Drying at room temperature is rather slow, since the boiling

Received: July 4, 2014
Accepted: October 15, 2014
Published: October 15, 2014

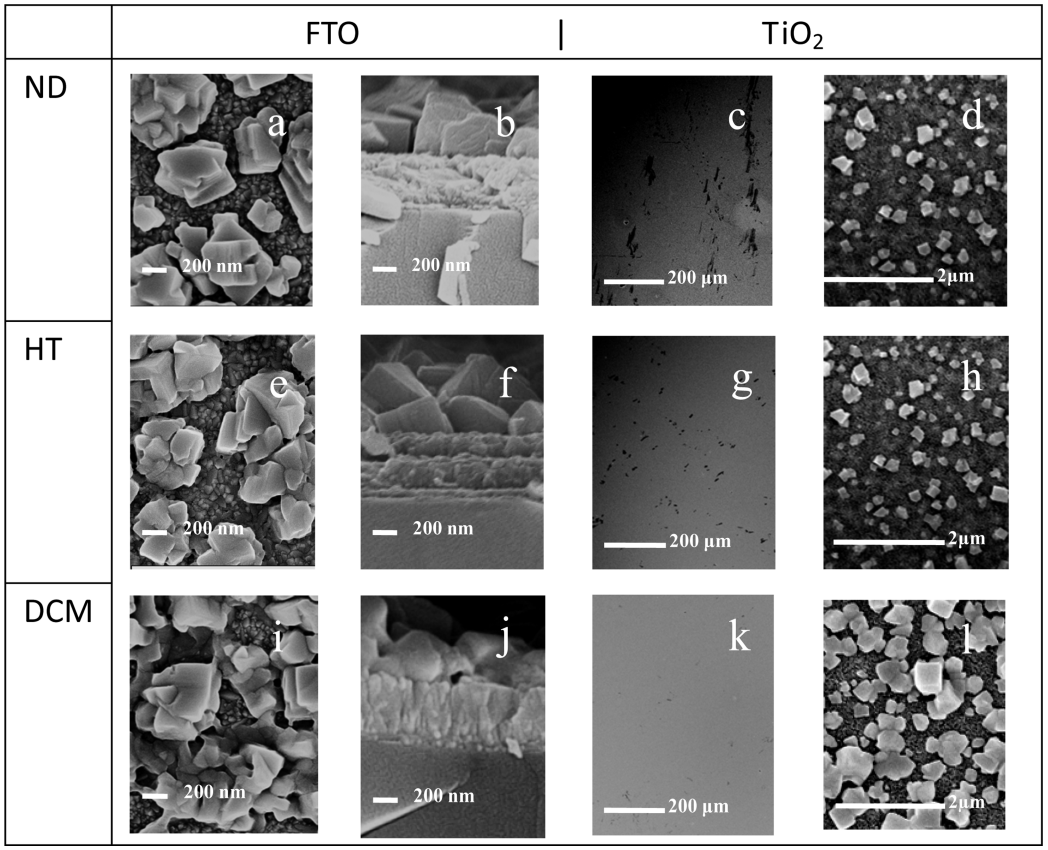

Figure 1. Top and sideview SEM pictures of $CH_3NH_3PbI_3$ on FTO substrates (two leftmost columns) and top view SEM pictures of $CH_3NH_3PbI_3$ on mesoporous TiO_2 (400 nm)/FTO (two rightmost columns). Panels a–d, ND treatment; panels e–h, HT treatment; and panels i–l, DCM treatment.

point of IPA is 82.5 °C. Therefore, drying at higher temperatures is preferred, but may not be ideal either. Here, we include a dichloromethane (DCM) treatment for the $CH_3NH_3PbI_3$ film directly after washing with IPA. $CH_3NH_3PbI_3$ and PbI_2 do not dissolve in DCM, and since the boiling point of DCM is only 39.6 °C, drying is very rapid. We found that this step greatly improves the $CH_3NH_3PbI_3$ film quality. We systematically compared DCM treatment with other two conditions: natural drying at room temperature (ND) after IPA washing, and drying at high temperature (100 °C) directly after IPA washing (HT). A final heat treatment on a hot plate set at 100 °C for 20 min in air was applied to all samples. The results demonstrate that DCM treatment helps to make a more-uniform perovskite film, in which charge recombination is reduced and with enhanced charge transport, leading to highly efficient and more-reproducible solar cells.

To investigate the effect of the different treatments on $CH_3NH_3PbI_3$ film morphology, we first prepared $CH_3NH_3PbI_3$ films on bare fluorine-doped tin oxide (FTO)-coated glass substrates, followed by different drying processes: ND, HT, and DCM. From the top view picture of $CH_3NH_3PbI_3$/FTO (see Figures 1a, 1e, 1i), it is evident that the $CH_3NH_3PbI_3$ films do not completely cover the FTO substrates. Using DCM treatment, however, leads to higher coverage compared to the other two drying processes. Furthermore, the formed crystals appear smoother and are interconnected by amorphous-looking material. In the ND and HT treatments, it appears that the thin layer that connects larger crystals is etched away, and sharper crystal edges can be seen. The reason may be that the perovskite film wetted with IPA in the ND and HT treatment can dissolve this part of the $CH_3NH_3PbI_3$ deposit.

$CH_3NH_3PbI_3$ films prepared on mesoporous TiO_2 substrates are shown in Figure 1 on the right-hand side. Under low magnification, it is apparent that the DCM-treated perovskite film (Figure 1k) gives the most uniform coverage of the substrate. The other two films show many defects, which may be harmful for solar cells. Under higher magnification (Figures 1d, 1h, 1l), it can be seen that the DCM treatment leads to a significantly higher coverage of the perovskite crystal overlayer. Good coverage of the perovskite on top of the TiO_2 also suggests a good penetration into the mesopores of the TiO_2 film, although we do not have direct evidence for this. Good coverage is important, as this will reduce direct contact between the spiro-OMeTAD hole transporting layer and the TiO_2 porous and compact layer. Any such contact can act as a shunting path, giving a shunting resistor (or diode) in the solar cell equivalent circuit, causing a drop in open-circuit potential (V_{oc}) and fill factor (FF), and leading to lower power conversion efficiencies.[23] The thickness of the perovskite crystal overlayer on TiO_2 film will be dependent on the thickness of the mesoporous TiO_2 film, where a thinner TiO_2 film results in a thicker perovskite top layer. The DCM treatment leads to perovskite crystals that are relatively bigger and much smoother than in the other two samples on TiO_2. Under the conditions used here, the perovskite crystal size was ~200–300 nm for the ND- and HT-treated samples and 200–500 nm for the DCM-treated sample.

Figure 2 shows X-ray diffraction (XRD) patterns of the perovskite $CH_3NH_3PbI_3$ using different treatments. When PbI_2 is deposited on TiO_2, it shows four peaks, which are attributed to the (001), (100), (110), and (111) lattice planes of a hexagonal (2H polytype) (Inorganic Crystal Structure Database, collection code 68819). The predominant peak of (001) indicates that PbI_2 grows in a preferential orientation along the *c*-axis of the TiO_2 film. After dipping the PbI_2 into the CH_3NH_3I solution, a new series of new diffraction peaks is observed that is in good agreement with literature data of the tetragonal phase of $CH_3NH_3PbI_3$ perovskite.[29] When comparing the three perovskite samples, a small peak in the ND sample is found (indicated by a red arrow in Figure 2), attributed to the (001) lattice plane of (2H) PbI_2. The presence of PbI_2 in this sample might be due to incomplete reaction of PbI_2 with CH_3NH_3I, but as the same procedure to transform PbI_2 into perovskite is used for all three samples (with no evidence for PbI_2 in HT and DCM samples), this is unlikely. Instead, partial dissolution of $CH_3NH_3PbI_3$ in IPA during the relatively slow drying process for ND samples seems to be the most plausible explanation for the presence of PbI_2. CH_3NH_3I is highly soluble in IPA, while PbI_2 has limited solubility.

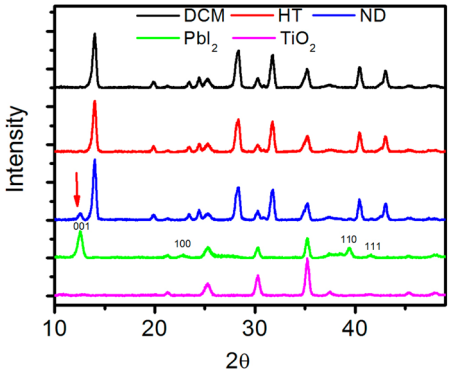

Figure 2. X-ray diffraction (XRD) patterns of mesoporous TiO_2, PbI_2/TiO_2, and $CH_3NH_3PbI_3/TiO_2$ with different drying treatments on ITO substrates.

In Figure 3, the photovoltaic performance of champion solar cells from the three different treatments is shown. From the *J*–*V* characterization, it is found that DCM and HT solar cells perform significantly better than ND solar cells: the efficiencies are 13.5%, 12.4%, and 9.7% and the J_{sc} values are 21.5, 20.8, and 17.8 mA cm^{-2}, for the DCM, HT, and ND samples, respectively. The values reported here are for reverse potential scans from V_{oc} and 0 V with a scan rate of ~50 mV s^{-1} (in 5 mV steps with ca. 80 ms delay and 20 ms measurement period). No strong hysteresis effects are observed in these devices in *J*–*V* characterization. The forward scan of the DCM device is also shown in Figure 3a, yielding a slightly reduced efficiency of 12.9%. Statistical data from 12 solar cell devices for each treatment, shown in Supporting Information (Figure S1), demonstrates that the improvements caused by the different drying procedures are significant: the average efficiencies were 8.8%, 11.5%, and 12.4% for the ND, HT and DCM devices, respectively.

The IPCE spectra of these solar cells show a broad response from 350 nm to 800 nm, with maximum values close to 90% for the DCM solar cell (see Figure 3b). As no antireflective coating was present on these devices, this corresponds to ~100% absorbed photon-to-electron conversion efficiency. The integrated currents calculated from the IPCE spectra are 21.1, 20.1, and 17.6 mA cm^{-2} for the DCM-, HT-, and ND-treated samples, respectively, in good correspondence with the J_{sc} under simulated AM 1.5 illumination of 100 mW cm^{-2}. The ND device has clearly poorer IPCE response in the red region. This relatively poor red response means that more carriers that are produced by red light, which penetrates longer into the perovskite film, are lost. This would suggest that charge separation from the perovskite is dominant at the TiO_2 interface under operating conditions, rather than at the spiro-MeOTAD interface. However, emission studies (shown later) suggest the opposite. At this point, no definitive conclusions can be drawn.

The open circuit potential (V_{oc}) was also improved by the DCM treatment, where an average value of 0.97 V was recorded (vs 0.91 and 0.84 V for HT and ND, respectively), and a highest value of 1.02 V. In solid-state dye-sensitized solar cells, V_{oc} is determined by the difference between the quasi-Fermi level in TiO_2 under illumination and the oxidation potential of the hole transporting material.[30] In the mesostructured perovskite solar cells in this study, the three different treatments are not expected to affect the energy levels of the materials. Instead, the differences in V_{oc} are related to differences in recombination rates between the charge carriers. DCM devices show much higher J_{sc} values, compared to the ND devices, which may be due to better electron injection and/or hole extraction processes. This will be discussed below, in relation to the single photon counting measurements. The fill factor (FF) of the DCM-treated device shows a value of 0.67, while lower values of FF = 0.64 and 0.62 are obtained for the HT- and ND-treated samples. The FF value is affected by both the shunt resistance and the series resistance in the device. The

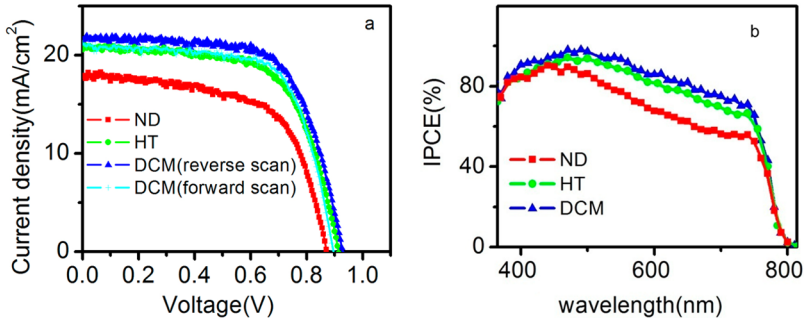

Figure 3. (a) *J*–*V* curves under AM 1.5 illumination of 100 mW cm^{-2} (using 50 mV s^{-1} to scan from V_{oc} to J_{sc} (reverse scan) and J_{sc} to V_{oc} (forward scan) after a waiting time of 20 s at V_{oc}) and (b) IPCE spectra of $TiO_2/CH_3NH_3PbI_3$/Spiro-OMeTAD/Ag solar cells.

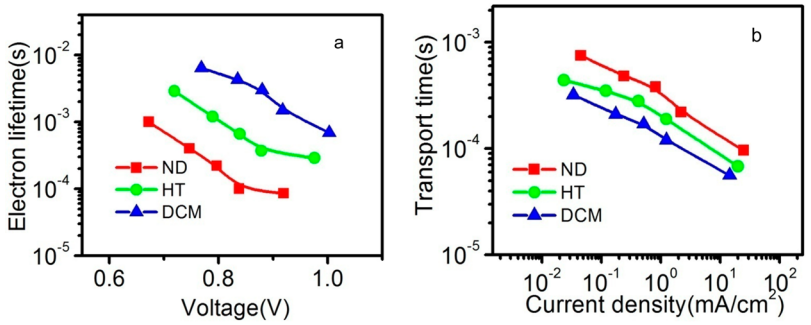

Figure 4. (a) Electron lifetime and (b) charge transport time of $TiO_2/CH_3NH_3PbI_3$/spiro-OMeTAD/Ag solar cells.

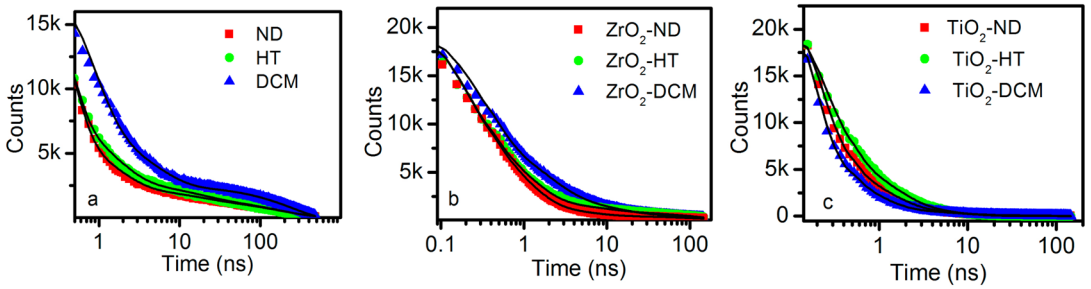

Figure 5. Emission kinetic decays of different perovskite samples on (a) glass, (b) TiO_2, and (c) ZrO_2, measured by time-correlated single-photon counting (TCSPC).

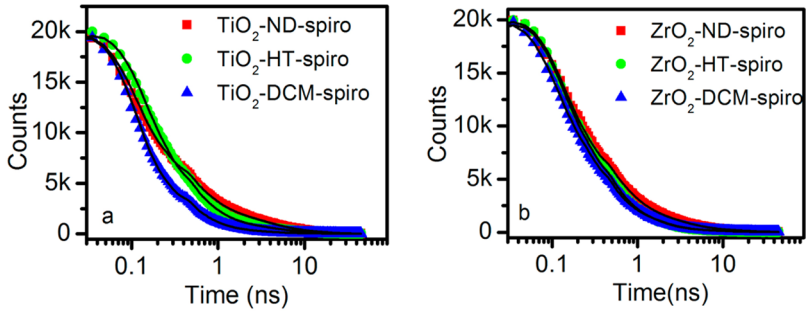

Figure 6. Emission kinetic decays measured by TCSPC of the different perovskite samples on (a) TiO_2 and (b) ZrO_2 substrates with spiro-MeOTAD.

latter can be linked to resistance of the FTO substrate, contact resistance, and the resistance of the hole transport material (HTM),[31] all of which should be similar for all three types of devices here. However, the shunt resistance is lower for the ND devices, as is evident from the higher slope of the current-potential ($I-V$) curve near 0 V, and results in lower solar cell performance. The low shunt resistance is attributed to poorer perovskite coverage of the TiO_2 in ND solar cells.

The charge transport and recombination in these three types of solar cells was studied in detail using transient small-modulation V_{oc} and J_{sc} decay measurements, from which the carrier lifetimes and transport times (t_{tr}) were derived. The results are shown in Figure 4. There are significantly longer carrier lifetimes in the DCM device, followed by HT and finally ND, which has carrier lifetimes ~1 order of magnitude shorter. The measured V_{oc} is given by the difference in the quasi-Fermi level ($E_{F,n}$) of TiO_2, and thus on the electron concentration in TiO_2 on one side,[32−34] and the Fermi level of the p-contact spiro-MeOTAD/Ag on the other side. We will assume here, based on the similarities of these devices to solid-state dye-sensitized solar cells, that the Fermi level of the p-contact is constant, due to the high doping level of spiro-MeOTAD, and that differences in V_{oc} are solely due to the electron concentration variations in the TiO_2. The measured transient voltage measurements therefore reflects the electron lifetime τ_e, which is considered as the average time for survival of free and trapped electrons in TiO_2 before recombination.[35] The recombination in the perovskite devices that is measured is that between electrons in the TiO_2 that recombine with the holes in the perovskite or in spiro-OMeTAD. Since electron injection in TiO_2 from perovskite is reported to be ultrafast, and the charge transport in TiO_2 mesostructure perovskite solar cells is relatively slow and similar to that in solid-state dye-sensitized solar cells, we can assume that electrons are mostly located in and recombine from the TiO_2 mesostructure.

The order for the transport times is $t_{tr,DCM} < t_{tr,HT} < t_{tr,ND}$, which is the reverse order than expected, compared to the electron lifetimes (see Figure 4). The transport times (recorded under short-circuit conditions) of the DCM devices are ~1 order of magnitude smaller than the electron lifetimes (recorded under open-circuit conditions) under the same illumination conditions. This strongly suggests that the charge collection efficiency is close to 100% for the DCM devices. For the other devices, the transport times are closer to the electron

lifetimes, suggesting that charge collection losses can occur, especially in the ND devices. The faster electron transport times for DCM devices seems to be correlated to the better coverage of TiO_2 with perovskite in this preparation.

Finally, time-correlated single-photon counting (TCSPC) was used to investigate the photoinduced carrier kinetics inside the perovskite material. Excitation laser pulses of 404 nm was used with a very low intensity (15 pJ/pulse at max.) to avoid Auger recombination that has been detected previously in $CH_3NH_3PbI_3$.[36] The emission decays of perovskite samples on different substrates, glass, TiO_2 and ZrO_2, are shown in Figures 5 and 6. The emission decay traces are clearly multiexponential and were fitted using a three-exponential function. Approximately 90% of the total amplitude of the lifetimes for the three samples is mainly associated with the first two lifetimes (see Supporting Information (Table S2). TCSPC emission measurements of perovskite samples reported previously gave monoexponential or biexponential decays with a time constants of 5.6 ns[36] and 9.6 ns[37] for $CH_3NH_3PbI_3$, and 283 ns for $CH_3NH_3PbCl_xI_{3-x}$.[37] The reason for different values can be attributed to different perovskite preparation procedures or measurement conditions (under vacuum or in air).

For the sake of clarity and simplicity, we used an amplitude-weighted lifetime $\langle\tau\rangle$[38] and will refer to it as the emission lifetime. Figure 5a shows emission decays of neat perovskite samples on glass, where no electron or hole injection can take place. The ND and HT samples have very similar kinetics with a lifetime of ~10 ns, while the DCM sample has a much longer lifetime of 39.0 ns, a remarkable 4-fold increase (see Table 1).

Table 1. Amplitude-Weighted Lifetimes $\langle\tau\rangle$ for the Emission Decays of Perovskite Samples and Calculated Quantum Efficiencies for Carrier Separation (η_{CS}), as Discussed in the Text

	ND		HT		DCM	
sample type	$\langle\tau\rangle$ (ns)	η_{CS}	$\langle\tau\rangle$ (ns)	η_{CS}	$\langle\tau\rangle$ (ns)	η_{CS}
on glass	9.72		9.75		39.0	
on ZrO_2	2.1		5.0		5.6	
on TiO_2	0.46	0.78	0.66	0.87	0.35	0.94
on ZrO_2/Spiro	0.34	0.84	0.21	0.96	0.18	0.97
on TiO_2/Spiro	0.32	0.85	0.31	0.94	0.13	0.98

Assuming that the morphology of the perovskite layer is similar to that on FTO substrates (see Figure 2), this observation may be explained by assuming that use of DCM in the drying process prevents the formation of defect sites that promote recombination.

Figure 5b shows the emission decay of the perovskite samples on mesostructured ZrO_2. Although ZrO_2 should be an inert interface, since no electron injection from the perovskite can occur, because of its high lying conduction band, we observe a decrease in emission lifetime for the DCM sample from 39.0 ns on glass to 5.6 ns on ZrO_2. Such a difference between the emission decays of perovskite on glass and a metal oxide insulator was recently shown for Al_2O_3 and was attributed to interactions at the perovskite/metal oxide interface.[39] It should also be noted that the perovskite material inside the mesoporous scaffold consist of much smaller crystallites than the overstanding perovskite layer. Because of the similarity of ZrO_2 and TiO_2 as mesoporous scaffold, we will consider the ZrO_2/perovskite samples as the reference for emission lifetime in perovskite in solar cell device configuration, in the absence of carrier injection. For the perovskite on ZrO_2, the ND samples gave the shortest emission lifetimes, but the difference between the HT and DCM samples was small.

By switching the mesostructure from ZrO_2 to TiO_2, the observed emission kinetics for all three samples become faster, which is attributed to ultrafast electron injection from the perovskite into TiO_2 (see Table 1, as well as Figure 5c). The DCM sample shows a distinct faster decay on TiO_2 than on ZrO_2, where the emission lifetime changed from 5.6 ns on ZrO_2 to 0.35 ns on TiO_2. From these measurements, an electron injection time constant (τ_{inj}) from perovskite into TiO_2 of ~0.37 ns is calculated using $(\tau_{inj})^{-1} = (\tau_{TiO_2})^{-1} - (\tau_{ZrO_2})^{-1}$, which is a factor of 2 less than that observed for the other two samples (for ND, 0.59 ns; for HT, 0.76 ns). The higher J_{sc} value of DCM devices can be attributed in part to faster electron injection, leading to higher charge collection efficiency for carriers from the perovskite to the selective contacts. This charge collection efficiency (η_{CS}) can be estimated from the TCSPC experiments using $\eta_{CS} = 1 - (\tau_{TiO_2}/\tau_{ZrO_2})$, showing that 94% of the photogenerated electrons are transferred to TiO_2. A recent kinetic study of perovskite on TiO_2 and Al_2O_3 showed similar kinetics on both semiconductors,[16] which is different from our observations. It must be emphasized that the preparation method for the perovskite may strongly affect the observed kinetics.

Addition of the hole transporting material spiro-OMeTAD has a significant effect on the charge separation in the solar cell. The TCSPC measurements clearly show that the spiro-OMeTAD/perovskite contact is also an active interface for charge separation. All the prepared samples show a faster emission quenching in the presence of Spiro-OMeTAD (see Table 1). The DCM sample shows the fastest emission decay (on TiO_2, 130 ps, compared to ~310 ps for ND and HT), which seems to be caused by more efficient/rapid hole injection. Analysis of the TSCPC data suggests that the DCM treatment favors both electron and hole injection at the respective contacts, while the ND and HT samples show similar, slower kinetics. The calculated charge collection efficiency from perovskite to either contact suggests significant current losses (~10%) for the ND device, which agrees well with the solar cell results.

In summary, we have demonstrated the critical role of the drying process in the two-step preparation method for $CH_3NH_3PbI_3$ perovskite films for highly efficient solar cells. By modifying the drying process, the morphology of perovskite films is affected and reproducible high efficiencies (up to 13.5%) were achieved. Best results were obtained when a dichloromethane dip and drying process was included. This avoids partial dissolution of the perovskite in the isopropanol rinsing/drying process and seems to lead to passivation of the semiconductor material, leading to enhanced charge injection, improved charge separation, and decreased charge recombination.

METHODS

A 50-nm compact TiO_2 blocking layer was first deposited onto the surface of a precleaned FTO substrate by spray pyrolysis on a hot plate at 500 °C, using a solution of 0.2 M Ti-isopropoxide and 2 M acetylacetone in isopropanol. The mesoporous layer TiO_2 was deposited by spin-coating a diluted paste (Dyesol 18NR-T), followed by heating to 450 °C. PbI_2 (Alfa Aesar, 99.9985% purity) is deposited via spin coating from a solution 1 mol/L PbI_2 in dimethylformamide (DMF) that is heated to 70 °C, with a spin-coating speed of 7000 rpm.

$CH_3NH_3PbI_3$ was formed by dipping the slide into a 10 mg/mL CH_3NH_3I in isopropanol (IPA) solution for 30 s, as is described in ref 20. The perovskite films were washed using IPA, followed by three different treatments, as described in the text. After removing the excess IPA, The perovskite films were then placed on a hot plate set at 100 °C for 20 min in air. The composition of hole transport material was 0.170 M 2,2′,7,7′-tetrakis(*N*,*N*-di-*p*-methoxyphenyl-amine)-9,99-spirobifluorene (spiro-OMeTAD, Lumtec), with the addition of 60 mM bis(trifluoromethane)sulfonimide lithium salt (LiTFSI, 99.95%, Aldrich) and 200 mM 4-*tert*-butylpyridine (TBP, 99%, Aldrich). The $CH_3NH_3PbI_3/TiO_2$ films were coated with HTM solution using the spin-coating method at 4000 rpm. For the electrical contact, a 200-nm Ag film was deposited onto the solar cell by thermal evaporation.

Characterization methods are described in the Supporting Information.

■ ASSOCIATED CONTENT

Supporting Information

Characterization methods; photovoltaic parameters of 36 solar cells; fitting parameters of emission decay. This material is available free of charge via the Internet at http://pubs.acs.org.

■ AUTHOR INFORMATION

Corresponding Author

*E-mail: gerrit.boschloo@kemi.uu.se.

Notes

The authors declare no competing financial interest.

■ ACKNOWLEDGMENTS

We thank the Swedish Energy Agency, the Swedish Research Council (VR), the STandUP for Energy program, and the Knut and Alice Wallenberg Foundation for financial support.

■ REFERENCES

(1) Green, M. A.; Emery, K.; Hishikawa, Y.; Warta, W.; Dunlop, E. D. Solar Cell Efficiency Tables (version 40). *Prog. Photovoltaics* **2012**, *20*, 606−614.

(2) Hagfeldt, A.; Boschloo, G.; Sun, L.; Kloo, L.; Pettersson, H. Dye-Sensitized Solar Cells. *Chem. Rev.* **2010**, *110*, 6595−6663.

(3) Branker, K.; Pathak, M. J. M.; Pearce, J. M. A Review of Solar Photovoltaic Levelized Cost of Electricity. *Renewable Sustainable Energy Rev.* **2011**, *15*, 4470−4482.

(4) Shah, A.; Torres, P.; Tscharner, R.; Wyrsch, N.; Keppner, H. Photovoltaic Technology: The Case for Thin-Film Solar Cells. *Science* **1999**, *285*, 692−698.

(5) Yella, A.; Lee, H. W.; Tsao, H. N.; Yi, C. Y.; Chandiran, A. K. Porphyrin-Sensitized Solar Cells with Cobalt (II/III)-Based Redox Electrolyte Exceed 12% Efficiency. *Science* **2011**, *334*, 1203−1203.

(6) Yu, G.; Gao, J.; Hummelen, J. C.; Wudl, F.; Heeger, A. J. Polymer Photovoltaic Cells—Enhanced Efficiencies Via a Network of Internal Donor−Acceptor Heterojunctions. *Science* **1995**, *270*, 1789−1791.

(7) Semonin, O. E.; Luther, J. M.; Choi, S.; Chen, H. Y.; Gao, J. B.; Nozik, A. J.; Beard, M. C. Peak External Photocurrent Quantum Efficiency Exceeding 100% via MEG in a Quantum Dot Solar Cell. *Science* **2011**, *334*, 1530−1533.

(8) Snaith, H. J. Estimating the Maximum Attainable Efficiency in Dye-Sensitized Solar Cells. *Adv. Funct. Mater.* **2010**, *20*, 13−19.

(9) Research Cell Efficiency Records. NREL (http://www.nrel.gov/ncpv/images/efficiency_chart.jpg), accessed on Oct. 15, 2014.

(10) Kitazawa, N.; Enomoto, K.; Aono, M.; Watanabe, Y. Optical Properties of $(C_6H_5C_2H_4NH_3)(2)PbI_{(4-x)}Br_{(x)}$ (x = 0−4) Mixed-Crystal Doped PMMA Films. *J. Mater. Sci.* **2004**, *39*, 749−751.

(11) Era, M.; Hattori, T.; Taira, T.; Tsutsui, T. Self-Organized Growth of PbI-Based Layered Perovskite Quantum Well by Dual-Source Vapor Deposition. *Chem. Mater.* **1997**, *9*, 8−10.

(12) Liang, K. N.; Mitzi, D. B.; Prikas, M. T. Synthesis and Characterization of Organic−Inorganic Perovskite Thin Films Prepared using a Versatile Two-Step Dipping Technique. *Chem. Mater.* **1998**, *10*, 403−411.

(13) Pradeesh, K.; Baumberg, J. J.; Prakash, G. V. In Situ Intercalation Strategies for Device-Quality Hybrid Inorganic−Organic Self-Assembled Quantum Wells. *Appl. Phys. Lett.* **2009**, *95*, 033309.

(14) Xia, Y. N.; Whitesides, G. M. Soft lithography. *Annu. Rev. Mater. Sci.* **1998**, *28*, 153−184.

(15) Cheng, Z. Y.; Lin, J. Layered Organic−Inorganic Hybrid Perovskites: Structure, Optical Properties, Film Preparation, Patterning and Templating Engineering. *CrystEngComm* **2010**, *12*, 2646−2662.

(16) Kim, H. S.; Lee, C. R.; Im, J. H.; Lee, K. B.; Moehl, T.; Marchioro, A.; Moon, S. J.; Humphry-Baker, R.; Yum, J. H.; Moser, J. E.; Gratzel, M.; Park, N. G. Lead Iodide Perovskite Sensitized All-Solid-State Submicron Thin Film Mesoscopic Solar Cell with Efficiency Exceeding 9%. *Sci. Rep.* **2012**, *2*, 591.

(17) Bi, D.; Yang, L.; Boschloo, G.; Hagfeldt, A.; Johansson, E. M. J. Effect of Different Hole Transport Materials on Recombination in $CH_3NH_3PbI_3$ Perovskite-Sensitized Mesoscopic Solar Cells. *J. Phys. Chem. Lett.* **2013**, *4*, 1532−1536.

(18) Lee, M. M.; Teuscher, J.; Miyasaka, T.; Murakami, T. N.; Snaith, H. J. Efficient Hybrid Solar Cells Based on Meso-Superstructured Organometal Halide Perovskites. *Science* **2012**, *338*, 643−647.

(19) Liu, M. Z.; Johnston, M. B.; Snaith, H. J. Efficient Planar Heterojunction Perovskite Solar Cells by Vapour Deposition. *Nature* **2013**, *501*, 395−398.

(20) Burschka, J.; Pellet, N.; Moon, S. J.; Humphry-Baker, R.; Gao, P.; Nazeeruddin, M. K.; Gratzel, M. Sequential deposition as a route to high-performance perovskite-sensitized solar cells. *Nature* **2013**, *499*, 316−320.

(21) Bi, D. Q.; Moon, S. J.; Haggman, L.; Boschloo, G.; Yang, L.; Johansson, E. M. J.; Nazeeruddin, M. K.; Gratzel, M.; Hagfeldt, A. Using a Two-Step Deposition Technique to Prepare Perovskite ($CH_3NH_3PbI_3$) for Thin Film Solar Cells based on ZrO_2 and TiO_2 Mesostructures. *RSC Adv.* **2013**, *3*, 18762−18766.

(22) Chen, Q.; Zhou, H.; Hong, Z.; Luo, S.; Duan, H.-S.; Wang, H.-H.; Liu, Y.; Li, G.; Yang, Y. Planar Heterojunction Perovskite Solar Cells via Vapor-Assisted Solution Process. *J. Am. Chem. Soc.* **2013**, *136*, 622−625.

(23) Eperon, G. E.; Burlakov, V. M.; Docampo, P.; Goriely, A.; Snaith, H. J. Morphological Control for High Performance, Solution-Processed Planar Heterojunction Perovskite Solar Cells. *Adv. Funct. Mater.* **2014**, *24*, 151−157.

(24) Liu, D.; Kelly, T. L. Perovskite Solar Cells with a Planar Heterojunction Structure Prepared using Room-Temperature Solution Processing Techniques. *Nat. Photonics* **2014**, *8*, 133−138.

(25) Ball, J. M.; Lee, M. M.; Hey, A.; Snaith, H. J. Low-Temperature Processed Meso-Superstructured to Thin-Film Perovskite Solar Cells. *Energy Environ. Sci.* **2013**, *6*, 1739−1743.

(26) Heo, J. H.; Im, S. H.; Noh, J. H.; Mandal, T. N.; Lim, C. S.; Chang, J. A.; Lee, Y. H.; Kim, H. J.; Sarkar, A.; Nazeeruddin, M. K.; Gratzel, M.; Seok, S. I. Efficient Inorganic-Organic Hybrid Heterojunction Solar Cells Containing Perovskite Compound and Polymeric Hole Conductors. *Nat. Photonics* **2013**, *7*, 487−492.

(27) Wang, J. T.-W.; Ball, J. M.; Barea, E. M.; Abate, A.; Alexander-Webber, J. A.; Huang, J.; Saliba, M.; Mora-Sero, I.; Bisquert, J.; Snaith, H. J.; Nicholas, R. J. Low-Temperature Processed Electron Collection Layers of Graphene/TiO_2 Nanocomposites in Thin Film Perovskite Solar Cells. *Nano Lett.* **2013**, *14*, 724−730.

(28) Laban, W. A.; Etgar, L. Depleted Hole Conductor-Free Lead Halide Iodide Heterojunction Solar Cells. *Energy Environ. Sci.* **2013**, *6*, 3249−3253.

(29) Baikie, T.; Fang, Y. N.; Kadro, J. M.; Schreyer, M.; Wei, F. X.; Mhaisalkar, S. G.; Graetzel, M.; White, T. J. Synthesis and Crystal Chemistry of the Hybrid Perovskite $(CH_3NH_3)PbI_3$ for Solid-State Sensitised Solar Cell Applications. *J. Mater. Chem. A* **2013**, *1*, 5628−5641.

(30) Cowan, S. R.; Leong, W. L.; Banerji, N.; Dennler, G.; Heeger, A. J. Identifying a Threshold Impurity Level for Organic Solar Cells:

Enhanced First-Order Recombination via Well-Defined $PC_{84}BM$ Traps in Organic Bulk Heterojunction Solar Cells. *Adv. Funct. Mater.* **2011**, *21*, 3083−3092.
(31) Abate, A.; Leijtens, T.; Pathak, S.; Teuscher, J.; Avolio, R.; Errico, M. E.; Kirkpatrik, J.; Ball, J. M.; Docampo, P.; McPherson, I.; Snaith, H. J. Lithium Salts as "Redox Active" P-Type Dopants for Organic Semiconductors and Their Impact in Solid-State Dye-Sensitized Solar Cells. *Phys. Chem. Chem. Phys.* **2013**, *15*, 2572−2579.
(32) De Greve, K.; Yu, L.; McMahon, P. L.; Pelc, J. S.; Natarajan, C. M.; Kim, N. Y.; Abe, E.; Maier, S.; Schneider, C.; Kamp, M.; Hofling, S.; Hadfield, R. H.; Forchel, A.; Fejer, M. M.; Yamamoto, Y. Quantum-Dot Spin-Photon Entanglement via Frequency Downconversion to Telecom Wavelength. *Nature* **2012**, *491*, 421−425.
(33) Gao, W. B.; Fallahi, P.; Togan, E.; Miguel-Sanchez, J.; Imamoglu, A. Observation of Entanglement Between a Quantum Dot Spin and a Single Photon. *Nature* **2012**, *491*, 426−430.
(34) Lewis, N. S. A Novel Solar-Cell. *Nature* **1983**, *305*, 671−671.
(35) Licht, S.; Hodes, G.; Tenne, R.; Manassen, J. A Light-Variation Insensitive High-Efficiency Solar-Cell. *Nature* **1987**, *326*, 863−864.
(36) Xing, G.; Mathews, N.; Sun, S.; Lim, S. S.; Lam, Y. M.; Grätzel, M.; Mhaisalkar, S.; Sum, T. C. Long-Range Balanced Electron-and Hole-Transport Lengths in Organic−Inorganic $CH_3NH_3PbI_3$. *Science* **2013**, *342*, 344−347.
(37) Stranks, S. D.; Eperon, G. E.; Grancini, G.; Menelaou, C.; Alcocer, M. J. P.; Leijtens, T.; Herz, L. M.; Petrozza, A.; Snaith, H. J. Electron-Hole Diffusion Lengths Exceeding 1 Micrometer in an Organometal Trihalide Perovskite Absorber. *Science* **2013**, *342*, 341−344.
(38) Lakowicz, J. R. *Principles of Fluorescence Spectroscopy*; Springer: New York, 2006.
(39) Roiati, V.; Colella, S.; Lerario, G.; De Marco, L.; Rizzo, A.; Listorti, A.; Gigli, G. Investigating Charge Dynamics in Halide Perovskite-Sensitized Mesostructured Solar Cells. *Energy Environ. Sci.* **2014**, *7*, 1889−1894.